Chinese Chemical Letters 33 (2022) 3981–3986

Contents lists available at ScienceDirect

Chinese Chemical Letters

journal homepage: www.elsevier.com/locate/cclet

Co-construction of advanced sulfur host by implanting titanium carbide into *Aspergillus niger* spore carbon

Rongfan Zhou[a], Shenghui Shen[a], Yu Zhong[a], Ping Liu[a], Yongqi Zhang[b,*], Lingjie Zhang[a,*], Xiuli Wang[a], Xinhui Xia[a,b,*], Jiangping Tu[a]

[a] *State Key Laboratory of Silicon Materials, Key Laboratory of Advanced Materials and Applications for Batteries of Zhejiang Province, and Department of Materials Science and Engineering, Zhejiang University, Hangzhou 310027, China*
[b] *Yangtze Delta Region Institute (Huzhou) & Institute of Fundamental and Frontier Science, University of Electronic Science and Technology of China, Huzhou 313000, China*

ARTICLE INFO

Article history:
Received 31 August 2021
Revised 17 October 2021
Accepted 7 November 2021
Available online 12 November 2021

Keywords:
Aspergillus niger
Spore carbon
Titanium carbide
Cathode
Lithium sulfur batteries

ABSTRACT

It is of great importance to directionally construct advanced carbon host to achieve high-performance carbon/sulfur cathodes for lithium sulfur batteries (LSBs). Herein, we report a unique hollow pumpkin-like carbon with notable rich-wrinkle microstructure and intrinsically dual doping with N&P elements *via* a facile annealing process of *Aspergillus niger* spore. Furthermore, highly conductive polar absorbents, TiC nanoparticles, are in situ implanted into the above *Aspergillus niger* spore carbon (ANSC) by carbothermal reaction, accordingly forming high-performance ANSC/TiC composite host for sulfur. Impressively, TiC nanoparticles play dual roles of not only pore formation in ANSC matrix but also enhancement of chemical absorption with polysulfides. With the positive synergistic effect between N&P co-doped ANSC matrix and TiC polar absorbent, the designed ANSC/TiC-S cathodes show unique advantages including larger accommodation space for sulfur, higher surface area, enhanced conductivity and better chemical absorption with soluble polysulfide intermediates. Consequently, the ANSC/TiC-S cathodes are endowed with good rate performance (496 mAh/g at 0.5 C) and enhanced long-term cycling stability (736 mAh/g with a capacity retention of 78.8% at 0.1 C after 100 cycles). Our research opens a new door to controllably design advanced composite cathodes from microorganisms for application in lithium sulfur batteries.

Building high-capacity and stable battery system is extremely critical for human beings to create a sustainable energy future. Among the current energy storage systems, lithium sulfur batteries (LSBs) have aroused tremendous attention worldwide due to high theoretical capacity (1675 mAh/g) of sulfur cathode and overwhelming energy density (2600 Wh/kg) [1–7]. However, there are still several problems to be settled in LSBs such as the poor electrical conductivity of sulfur and product Li_2S, unavoidable volumetric expansion/shrinkage as well as internal shuttle effect of polysulfide Li_2S_x ($4 \leq x \leq 8$), which severely hinder the practical applications of LSBs [8–13].

Over the past decades, plenty of works focused on modified lithium metal anode [6], separators [14], electrolyte under different states [7,15] and sulfur cathode [16] to improve the electrochemical performance of LSBs, in which various carbon-based materials (hollow carbon spheres [17], carbon nanotubes [18–21], graphene [4,21,22], *etc.*) have been investigated as sulfur hosts to improve the conductivity and restrain the shuttle effect during cycling process. Among these, carbon from bacterium and fungus precursors has attracted enormous attention in virtue of morphological diversity, high reproduction efficiency, and in situ heteroatoms doping [23–25]. Typically, theoretical calculations have suggested that the absorption energies of polysulfide intermediates on N&P dual doped carbon surface increase sharply with comparison to pure carbon materials [26]. Therefore, in situ heteroatom doping in carbon from bacterium and fungus makes great contribution to more polar sites to strengthen chemical interaction with Li_2S_x and thereby lower energy barrier to accelerate electrochemical kinetics [23,27,28]. For instance, our group pioneered N&P doped spore carbon produced from *Aspergillus oryzae* [29] and *Trichoderma* [30] as excellent sulfur hosts. Boosted capacity and cycling performance were proven in these systems. Beyond that, Wang *et al.* reported a hierarchical sulfur host composite with carbon from gram-positive bacteria bacillus subtilis (GBBS) [26]. However, the carbon from GBBS showed a small specific surface area (46.3 m^2/g) and low

* Corresponding authors.
E-mail addresses: yqzhang@uestc.edu.cn (Y. Zhang), zhanglingjie@zju.edu.cn (L. Zhang), helloxxh@zju.edu.cn (X. Xia).

https://doi.org/10.1016/j.cclet.2021.11.032
1001-8417/

accommodation space for sulfur loading. Instead, Xu *et al.* synthesized *Aspergillus flavus* conidia-derived carbon with overwhelming surface area of 2459.6 m^2/g as sulfur host, which delivered a high initial capacity of 1625 mAh/g at 0.2 C [31]. Nevertheless, the intense carcinogenicity of *Aspergillus flavus* as Class I Carcinogens threatens the entire production safety in large scale and therefore limits its practical applications in energy storage [32]. Based on this background, we turn our attention to spore carbon derived from *Aspergillus niger* with similar rich-wrinkle microstructure but no damage to human health [33,34]. *Aspergillus niger* spore has been applied extensively in fermentation industry due to its numerous advantages including high tolerance of pH and temperature, rapid reproduction velocity, low cost and ample metabolites [35,36], but hitherto there is no attempt to utilize *Aspergillus niger* spore carbon (ANSC) for electrochemical energy storage. It is worth noting that ANSC is extremely hopeful to be used as efficient carbon matrix for sulfur loading. On one hand, ANSC has a hollow pumpkin-like microstructure with plenty of wrinkles, which can physically hinder the shuttle of polysulfides. On the other hand, ANSC is inherently codoped by N&P elements, which result in enhanced chemical absorption with Li_2S_x to prevent the loss of active materials [5,37]. Therefore, more work should be devoted to controllable fabrication of ANSC and dig out their electrochemical performance.

In order to further compensate the nonpolar nature and limited doping amount of carbon, polar inorganics (for example, TiC [38–41], TiN [42], Co_2B [43], Ni_2P [44–46] and NbC [30,47]) are investigated as chemical absorbents in virtue of positive attributes such as high electronic conductivity and desirable chemisorptivity with polysulfides. Typically, titanium carbide (TiC) comes into view due to its notable polar property, low cost, steady structure and superior electronic conductivity of 10^5 S/m [48–50]. Furthermore, TiC nanoparticles can be compatibly implanted into carbon matrix with function of pore formation, which leads to better accommodation of active materials [46]. Consequently, it is favorable to construct highly porous conductive sulfur host by implanting TiC nanoparticles into N&P codoped ANSC. To the best of our knowledge, this combination has not been reported yet and their application in lithium sulfur batteries is waiting for disclosure.

In the present work, we report a novel hybrid structure with polar TiC nanoparticles implanted into N&P dual-doped ANSC matrix for sulfur accommodation. The as-synthesized N&P codoped ANSC exhibits unique hollow pumpkin-like porous structure. Additionally, TiC nanoparticles play dual roles of not only pore formation in ANSC matrix but also enhancement of chemical absorption with polysulfides. The synchronal pore formation effect is due to the carbothermal reaction. The electrochemical performance of ANSC/TiC-S composite cathode has been thoroughly studied and demonstrated good high rate capability (496 mAh/g at 0.5 C) and enhanced cycling stability (decay rate of 0.21% per cycle during 100 cycles at 0.1 C). The positive synergistic effect between TiC and ANSC leads to enhanced conductivity and physical/chemical blocking effect for polysulfides is mainly responsible for the performance enhancement. Our research further verifies that the collaborative design of metal carbide and mold carbon is effective to achieve advanced sulfur cathode for lithium sulfur batteries.

The overall schematic fabrication process and characterization of ANSC/TiC composite are demonstrated in Fig. 1a. We implanted highly conductive TiC nanoparticles into ANSC matrix to form a high-performance ANSC/TiC hybrid composite through a facile solvothermal-carbothermal (ST-CT) method. The morphology and composition information of ANSC are presented in scanning electron microscopy (SEM) and transmission electron microscopy-high resolution transmission electron microscopy (TEM-HRTEM) images in Figs. 1b-e and Fig. S1 (Supporting information). The ANSC sample was obtained *via* a facile carbonization process of *Aspergillus*

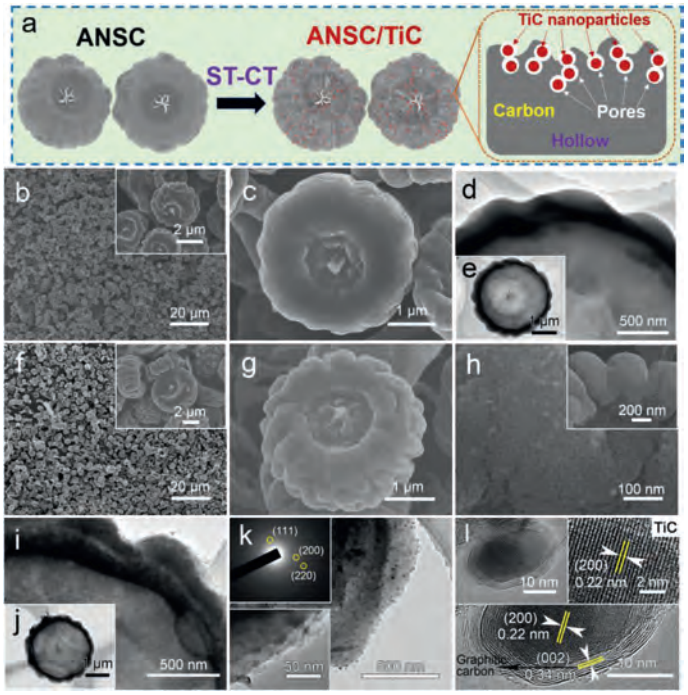

Fig. 1. Schematic fabrication process and characterization of ANSC and ANSC/TiC samples. (a) Schematic illustration of ANSC/TiC. (b, c) SEM images and (d, e) TEM images of ANSC. (f-h) SEM images, (i-k) TEM images (SAED patterns in inset) and (l) HRTEM images of ANSC/TiC composite.

niger spores at 800 °C in Ar atmosphere for 2 h. According to SEM images (Figs. 1b and c, Fig. S1a), the ANSC with an average diameter of 2-3 μm exhibits innovative pumpkin-like architecture with numerous wrinkles and relatively smooth surface. Detailed microstructure of ANSC is unraveled by TEM-HRTEM images as shown in Figs. 1d and e and Fig. S1b, which exhibit the pumpkin-like architecture of ANSC with hollow structure. Furthermore, the amorphous characteristic of ANSC is confirmed by HRTEM image and selected area electron diffraction (SAED) (inset in Fig. S1b) with unordered lattice fringe and unobvious diffraction spot, respectively. Meanwhile, because *Aspergillus niger* spores are comprised of organic matters such as proteins and polysaccharides [33], ANSC is *in situ* codoped by N&P after high-temperature carbonization treatment, which can be further verified by energy-dispersive X-ray spectroscopy (EDS) elemental mapping images (Fig. S1c) and X-ray photoelectron spectroscopy (XPS) analysis (Fig. S2 in Supporting information). The N 1s spectrum (Fig. S2a) shows three characteristic peaks of pyridinic-N and pyrrolic-N located at 397.5 eV and 399.8 eV respectively [51,52]. As for the P 2p spectrum (Fig. S2b, Supporting Information), it contains a typical peak of P-C located at 132.4 eV [29]. The doping of N and P elements can effectively enhance the electronic conductivity and adsorb the soluble polysulfide intermediates, which can synergistically boost electrochemical performance.

As we all known, large porosity and high conductivity and polarity are of great significance to enhance the physical and chemical absorptivity to polysulfides for the sulfur host [53,54]. As shown in the overall schematic fabrication process in Fig. 1a, the as-synthesized TiC nanoparticles are converted from ST-TiO_2 precursor at 1200 °C *via* the plausible reaction: $2C + TiO_2 \rightarrow TiC + CO_2$ (i) [55]. During the carbothermic reaction, the ST-TiO_2 nanoparticle precursor, uniformly dispersing on the surface of ANSC matrix, possess sufficient contact area with carbon to gradually consume carbon matrix material and meanwhile desorb CO_2 gas. According to the chemical equation (i), the con-

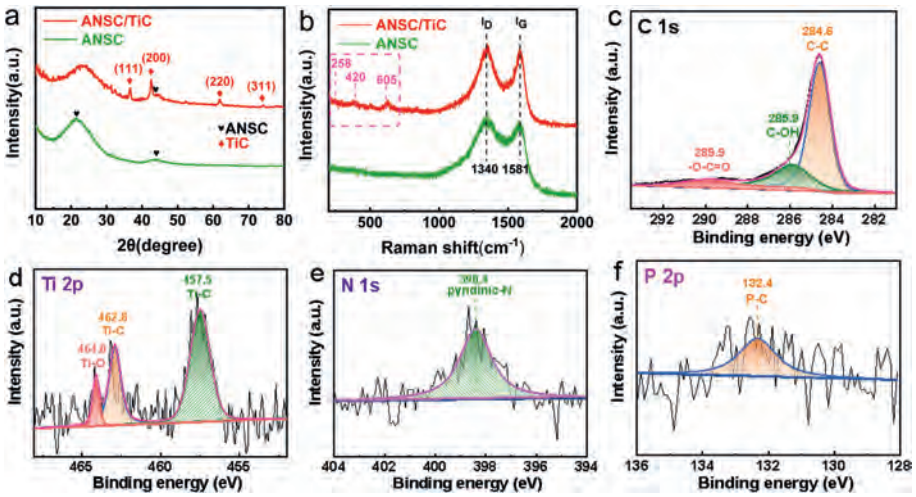

Fig. 2. Composition and structure characterizations of ANSC/TiC hybrid sample. (a) XRD patterns. (b) Raman spectra; XPS spectra: (c) C 1s spectrum, (d) Ti 2p spectrum, (e) N 1s spectrum and (f) P 2p spectrum.

sumed TiO_2 and C are converted to the ultimate solid product TiC with the equal mole, in which process the total volume decreases and gas is released to successfully form homogeneous pores. The as-obtained TiC nanoparticles exhibit an average diameter of 10-50 nm and are uniformly distributed in the ANSC matrix. From the thermogravimetric (TG) analysis (Fig. S7a in Supporting information), it can be calculated that the content of the as-synthesized TiC nanoparticles is about 14.2 wt%. Interestingly, this CT procedure possesses pore-formation effect, generating numerous pores in ANSC matrix to obtain the composite host with high porosity. The generated mesopores with the size range of 20-50 nm are distributed homogeneously around the TiC nanoparticles in the ANSC matrix (Figs. 1f-h). According to the Brunauer-Emmett-Teller (BET) test results (Fig. S3 in Supporting information), the ANSC-TiC composite exhibits a large specific area of 365 m^2/g, much higher than the pure ANSC (~171 m^2/g). Moreover, the pore size distribution of ANSC/TiC sample reveals that the ANSC/TiC composite is endowed with larger porosity, higher pore volume (0.142 cm^3/g of ANSC/TiC *vs*. 0.101 cm^3/g of ANSC) and optimized pore system with comparison to the pristine ANSC sample. The well distribution of the TiC nanoparticles and mesopores are also verified by TEM images as shown in Figs. 1i-k. During the whole process, the hollow pumpkin-like morphology is perfectly maintained. The obvious diffraction spots of ANSC/TiC SAED pattern (inset in Fig. 1k) are corresponding to (111), (200) and (220) crystal planes of TiC phase, confirming the polycrystalline nature of TiC nanoparticles [49]. Furthermore, TEM-HRTEM images in Fig. 1l verify the successful formation of TiC phase with clear lattice distance of 0.22 nm ascribed to TiC (200) lattice plane. The EDS elemental mappings (Fig. S5 in Supporting information) further illustrate the uniform distributions of C, N, P and Ti elements in the final ANSC/TiC hybrid composite structure. The synthetic work of in situ doped N&P elements and conductive TiC nanoparticles can effectively enhance the electronic conductivity, strengthen the polarity and improve the specific surface area, contributing to accelerated reaction kinetics and increased adsorption ability to the polysulfides. All these results indicate the advancement of ANSC/TiC hybrid composite as the high-performance sulfur host in LSBs.

X-ray diffraction (XRD), Raman spectrum and XPS tests shown in Fig. 2 demonstrate the detailed composition and structural information of ANSC/TiC hybrid composites. Fig. 2a displays the typical XRD patterns of ANSC and ANSC/TiC samples. The ANSC sample shows two typical broad peaks at 24° and 43° in agreement with (002) and (100) crystal planes of the amorphous carbon (JCPDS No. 75-1621) [56,57]. After ST-CT process, the ANSC/TiC sample shows several new characteristic peaks at 36°, 42°, 62° and 74°, matching well with (111), (200), (220) and (311) planes of TiC phase (JCPDS No. 32-1383) [58]. The above results provide strong evidence for the successful formation of TiC nanoparticles, also verified by Raman (Fig. 2b) and XPS tests (Figs. 2c-f). Both ANSC and ANSC/TiC samples show two typical Raman peaks located at 1340 and 1581 cm^{-1}, according with D-band and G-band of carbon materials [3]. As for the ANSC/TiC sample, another three characteristic peaks at 258, 420 and 605 cm^{-1} are observed in good agreement with TiC phase [49], indicating the successful preparation of TiC nanoparticles and ANSC matrix. Thus it is obvious of the superb compatibility and excellent synergistic effect between TiC and ANSC mutually. In terms of structure, the porous ANSC can provide larger space for sulfur accommodation and be endowed with more stable structure to avoid collapse due to the cubical dilatation during cycling. In terms of electrochemical performance, the TiC combination can promote both electroconductivity and physical & chemical dual adsorption with polysulfide intermediates to synergistically enhance reaction kinetics and reactivity. The surface chemical information and valence state of ANSC and ANSC/TiC were detected by XPS technique in wide-scan survey spectrum (Fig. S6 in Supporting information) and high-resolution spectra of C, Ti, N, and P elements (Figs. 2c-f). As for the C 1s spectrum (Fig. 2c), the ANSC/TiC sample exhibits four characteristic peaks of C–C (284.6 eV), C–OH (285.9 eV) and –O–C=O (289.9 eV), confirming the existence of TiC phase and hydrophilic oxygen functionalities [59]. As for the high-resolution Ti 2p spectrum (Fig. 2d), it can be deconvoluted into three peaks centered at 457.5, 462.8 and 464.8 eV, which are respectively assigned to Ti–C, Ti–C and Ti–O bonding [60], revealing the successful formation of TiC phase and the partial oxidation in the titanium family compounds. In addition, it is worth noting that the N 1s (Fig. 2e) and P 2p spectrum (Fig. 2f) are detected both in ANSC and ANSC/TiC composite. Slightly different to ANSC counterpart, the N 1s spectrum of ANSC/TiC can be fitted into only one component peak located at 398.4 eV, corresponding to pyridinic-N [51]. It is due to the transformation from volatile pyrrolic-N to pyridinic-N, which can especially enhance the chemical interaction with mobile polysulfide intermediates [61,62]. As for the P 2p spectrum, there exists one typical peak located at 132.4 eV, assigned to P-C bonding [29]. Additionally, the XPS results (Table S1 in Supporting information) reveal that the atomic content of N and P elements in ANSC/TiC are about 1.33 at% and 0.5 at%, respectively. According to the above results, after ST-CT procedure, the

doping N and P elements are well in situ distributed in ANSC/TiC composite. The cooperation of TiC and N&P heteroatoms can effectively enhance the intrinsic conductivity and provide more active sites to immobilize polysulfide intermediates, predicting its superior electrochemical properties.

To explore and compare the chemical adsorption capability of ANSC and ANSC-TiC samples towards polysulfide intermediates, the *ex situ* visible adsorption tests were conducted using pure Li_2S_6 solution as the representative for long-chain polysulfide species. ANSC and ANSC/TiC with the mass ratio as 2.13:1 were immersed in the same amount of 0.5 mmol/L Li_2S_6 solution for 24 h. Fig. S8 (Supporting information) shows that the depigmentation in ANSC/TiC sample is much faster than ANSC counterpart, indicating the higher "physical restriction" and "chemical absorption" to the long-chain polysulfides of ANSC/TiC composite due to the cooperation of TiC nanoparticles and N&P heteroatoms. The XPS characterizations in Fig. S9 (Supporting information) after Li_2S_6 adsorption test further reflect the main origin of polysulfide absorption capacity, which demonstrates the presence of C, N, P, S, Ti elements on the surface of the ANSC/TiC after soaking in polysulfide solution. As for the high-resolution Ti 2p spectrum after soaking (Fig. S9a), the two typical peaks located at 457.9 and 463.6 eV are assigned to the Ti-C bonding with positive position shifts of 0.4 and 0.8 eV. The positive shifts reveal that S with stronger electronegativity availably interacts with Ti atoms, leading to lone pair electrons of Ti deviating to S. The lower electron density of Ti atoms results in stronger bonding capability of nucleus. Another peak located at 455.5 eV is attributed to O-Ti-S bonding [59], consistent with the Ti-O bonding emerging in Fig. 2d before soaking, which further indicates the chemical interaction between ANSC/TiC composite and polysulfides. The N 1s spectrum shown in Fig. S9b exhibits two typical peaks located at 397.3 eV and 400.4 eV, respectively representing for pyridinic-N and pyrrolic-N. Similar to the analysis of Ti element, the negative position shift of pyridinic-N can be also considered to derived by the change of atomic chemical environment for N atoms, disclosing the chemical bonding between N and Li. In Fig. S9c, the P-C peak positively shift to 133.1 eV after soaking, indicating the effective interaction between P and S. The S 2p spectrum in Fig. S9d is another strong evidence for the polysulfides adsorption. Two characteristic peaks located at 163.5 and 164.9 eV represent for the terminal sulfur (S_T^{-1}) and bridging sulfur (S_B^0), respectively, exposing the successful adsorption of polysulfides on the surface of ANSC/TiC [63]. Another peak at 169.2 eV is ascribed to the polythionate species produced during the solution preparation [64,65]. All the above high-resolution XPS spectrum of Ti, N, P, S jointly clarify that both the N&P co-doping and TiC combination make contributions to the enhancement of chemical adsorption to polysulfides.

To explore the electrochemical application of ANSC/TiC as the sulfur host for LSBs, sulfur is infiltrated into ANSC/TiC and ANSC samples through a facile melt-diffusion method at 155°C for 12 h (Fig. 3a). The mass loading of sulfur in ANSC-S and ANSC/TiC-S electrodes was controlled at about 2 mg/cm^2. The morphology and composition information of ANSC-S and ANSC/TiC-S is demonstrated in SEM and TEM characterization in Figs. 3b-h and Figs. S4a-c. After sulfur incorporation, both samples perfectly maintain the pristine pumpkin-like structure. The sulfur is homogeneously accommodated in hosts and no aggregation of sulfur particles is detected. As for the ANSC/TiC-S sample (Figs. 3b-h), the surface becomes smoother and the generated mesopores are fulfilled with sulfur compared to the pristine ANSC/TiC counterpart (Fig. 1h), indicating that sulfur particles are successfully permeated into the pores to obtain higher sulfur loading. Meanwhile, the EDX elemental mapping analysis of ANSC/TiC-S (Fig. 3h) display the uniform distributions of C, N, P, Ti and S elements, indicating the successful accommodation of sulfur. According to the TG results (Fig. S7b in Supporting information), the sulfur content of ANSC/TiC-S (73.85 wt%) is notably higher than ANSC-S (68.85 wt%), implying that the accommodation ability to sulfur of ANSC/TiC is much higher than that of pristine ANSC due to its larger area and inner space. Moreover, XRD patterns of ANSC-S and ANSC/TiC-S in Fig. 4a show a series of characteristic peaks of sulfur (JCPDS No. 08-0247) [66], further confirming the successful introduction of sulfur into both hosts.

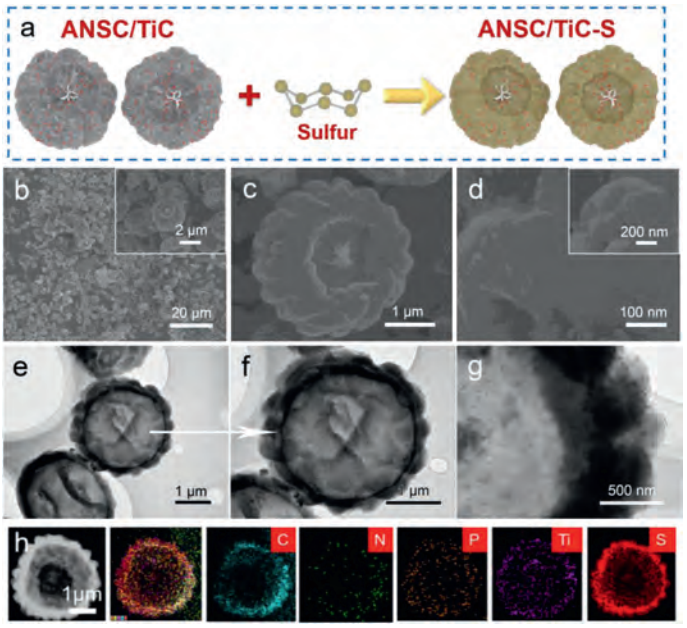

Fig. 3. Characterizations of ANSC/TiC-S sample. (a) Schematic fabrication process; (b-d) SEM images; (e-g) TEM images; (h) EDX elemental mapping images of C, N, P, Ti, S elements.

The as-synthesized ANSC-S and ANSC/TiC-S electrodes were applied as cathodes in LSBs to test the electrochemical properties. The CV curves (Fig. 4b) in the voltage rage of 1.7-2.8 V at 0.1 C distinctly unravel the enhancement of electrochemical performances for ANSC/TiC-S compared to ANSC-S. As for the cathodic process, both electrodes show two typical reductive peaks. The first reductive peak can be attributed to the solid-liquid electrochemical reaction of insoluble S converting into soluble long-chain Li_2S_x ($4 \leq x \leq 6$) and the liquid-liquid reaction from long-chain Li_2S_x to short-chain Li_2S_y, which is located at approximately 2.3 V. The second reductive peak can be ascribed to the liquid-solid conversion from short-chain Li_2S_y to insoluble Li_2S_2 or the ultimate discharge product Li_2S [67]. It is noteworthy that ANSC/TiC-S cathode shows lower anodic reaction potential and higher cathodic reaction potential, illustrating the lower polarization and better reaction reversibility of ANSC/TiC-S electrode in comparison to ANSC-S counterpart. To make the data transparent, differential CV plots at 1st and 5th cycle are provided (Fig. S10 in Supporting information) to distinguish the onset potentials, the peak current and relative voltage at reductive and oxidation peaks. According to the differential analysis, for the ANSC/TiC electrode, the peak current of the first reductive peak is –0.643 A/g and the onset potential of the second reductive peak is 2.12 V, higher than the corresponding values of ANSC electrode (−0.54 A/g, 2.09 V). The conclusion from the differential curves for the 5th cycle exhibits great consistence with the result from the 1st cycle, indicating the enhanced transformation kinetics and electrochemical reactivity of sulfur electrochemistry with TiC nanoparticles. Moreover, the higher peak current density and larger peak area further disclose the improved reaction kinetics of ANSC/TiC-S elec-

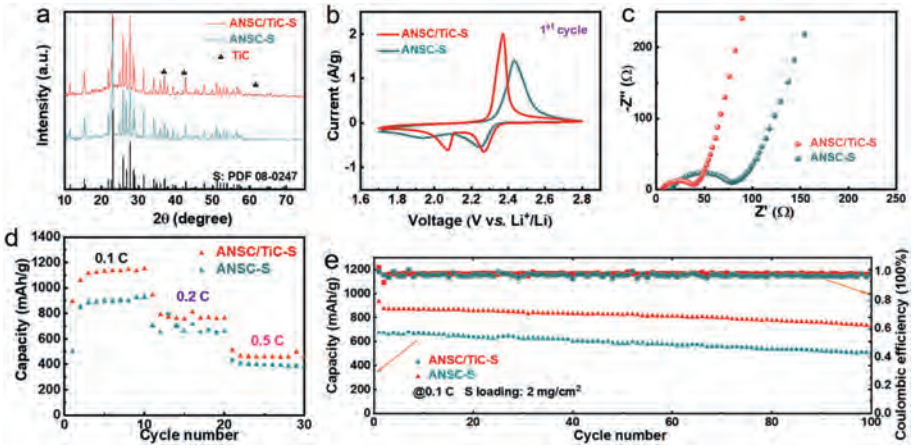

Fig. 4. Characterizations and electrochemical performance of ANSC-S and ANSC/TiC-S electrodes. (a) XRD patterns; (b) CV curves (1st at 0.1 mV/s); (c) Nyquist plots (inset: equivalent circuit diagram); (d) Rate performance; (e) Cycling performance.

trode. The electrochemical impedance spectroscopy (EIS) results in Fig. 4c demonstrate that the ANSC/TiC-S electrode has a much smaller charge transfer resistance (32.8 Ω) than ANSC-S counterpart (63.9 Ω), implying the improvement of redox reaction kinetics and charge-transfer capacity across cathode-electrolyte interface, which forecasts its higher electrochemical properties. The possible reasons favorable for fast energy storage are proposed as follows. On one hand, the hollow wrinkle-rich mesoporous architecture of ANSC/TiC can provide sufficient space for sulfur accommodation and release the volume change during charge/discharge process. On the other hand, doped N&P heteroatoms and TiC nanoparticles can effectively afford more active sites to anchor polysulfide intermediates and enhance the electronic conductivity of the composite host, which would effectively improve the cycling stability and accelerate the reaction kinetics during the electrochemical redox processes. Such an enhancement is confirmed by the results of rate performance subsequently. As expected, the ANSC/TiC-S cathode (Fig. 4d) delivers a much higher initial discharge capacity of 1059 mAh/g at 0.1 C than ANSC-S (850 mAh/g). In high-rate test, it still maintains overwhelming capacities of 1132 (0.1 C), 761 (0.2 C), 496 (0.5 C) mAh/g, respectively, superior to the ANSC-S counterpart of 893 (0.1 C), 714 (0.2 C), 392 (0.5 C) mAh/g and other biomass derived carbon hosts (Table S3 in Supporting information). Furthermore, the galvanostatic charge/discharge curves (Fig. S11 in Supporting information) at 0.1 C reveal smaller voltage drop and higher capacity, suggesting the enhanced reactivity and accelerated redox kinetics for ANSC/TiC-S cathode. The cycling performances are shown in Fig. 4e, in which the ANSC/TiC-S electrode maintains a high discharge capacity of 736 mAh/g (78.8% capacity retention) after 100 cycles at 0.1 C with low decay rate of 0.21% per cycle, superior to ANSC-S (Table S2 in Supporting information) and other biomass derived carbon materials (Table S3). All the above results can be attributed to the well-designed hollow pumpkin-like structure and cooperation of TiC nanoparticles as well as N&P heteroatoms in ANSC/TiC matrix.

To sum up, the overwhelming electrochemical performances of ANSC/TiC-S electrodes can be mainly attributed to the following synergistic functions of the porous pumpkin-like ANSC matrix, conductive TiC nanoparticles and codoped N and P heteroatoms: (1) The ANSC/TiC hybrid host with unique porous pumpkin-like structure and hollow characteristics provides large space for sulfur accommodation, which can effectively enhance the utilization of active material. Additionally, cross-linked wrinkles at the surface of ANSC can further build the continuous network for fast electron transportation and provide physical adsorption to the soluble polysulfides. (2) The dual-doped N and P heteroatoms in ANSC matrix provides enhanced electron conductivity and strong adsorption ability towards soluble polysulfides, which can effectively improve electrochemical reaction kinetics and suppress shuttle effects. (3) *In-situ* implanted conductive TiC nanoparticles further improve electronic/ionic conductivity of the hybrid host and anchor polysulfide intermediates as the chemical absorbents. Moreover, the polar TiC nanoparticles can also enhance the electrocatalytic activity during the charge/discharge processes, which can effectively decrease the passive overpotentials and improve the reaction kinetics, resulting in enhanced high-rate capacities and cycling stability.

In summary, for the first time, we have successfully developed an ingenious pumpkin-like hollow N and P-codoped ANSC/TiC hybrid composite *via* a facile combined solvothermal-carbothermal strategy. It is overwhelming that the homogeneously dispersed TiC nanoparticles show extraordinary compatibility with ANSC matrix and work as pore formation agent to create the porous architecture with large specific surface area of 365 m^2/g, demonstrating its superb accommodation potential for sulfur. The well-designed porous pumpkin-like architecture as well as the cooperation of the N&P heteroatoms and polar TiC nanoparticles effectively enlarge the specific surface area, improve electron/ion conductivity, and strengthen chemisorption and physisorption ability to polysulfide intermediates, indicating its superior electrochemical properties of LSBs with better high-rate performance (496 mAh/g at 0.5 C) and cycling stability (decay rate of 0.21% per cycle during 100 cycles at 0.1 C). The innovative combination between unique mold carbon and conductive metal carbide provides a new route for construction of advanced sulfur host for application in fast electrochemical energy storage and conversion.

Declaration of competing interest

The authors declare that they have no known competing financial interests or personal relationships that could have appeared to influence the work reported in this paper.

Acknowledgments

This work is supported by Natural Science Funds for Distinguished Young Scholars of Zhejiang Province (No. LR20E020001), National Natural Science Foundation of China (Nos. 52073252 and 51772272), and Foundation of State Key Laboratory of Coal Conversion (No. J20-21-909).

Supplementary materials

Supplementary material associated with this article can be found, in the online version, at doi:10.1016/j.cclet.2021.11.032.

References

[1] M. Li, W. Feng, X. Wang, Int. J. Electrochem. Sci. 15 (2020) 526–534.
[2] M. Ren, X. Lu, Y. Chai, et al., J. Colloid Interface Sci. 552 (2019) 91–100.
[3] X. Zhuang, Y. Liu, J. Chen, et al., J. Energy Chem. 23 (2014) 391–396.
[4] X. Zhu, W. Zhao, Y. Song, et al., Adv. Energy Mater. 8 (2018) 1800201.
[5] S.K. Liu, X.B. Hong, Y.J. Li, et al., Chin. Chem. Lett. 28 (2017) 412–416.
[6] J. Liu, H. Yuan, H. Liu, et al., Adv. Energy Mater. (2021) 2100748.
[7] Z. Xie, Y. Zhou, C. Ling, et al., Chin. Chem. Lett. 33 (2022) 1407–1411.
[8] Z. Wang, J. Shen, J. Liu, et al., Adv. Mater. 31 (2019) 1902228.
[9] S. Xia, X. Zhang, C. Liang, et al., Energy Stor. Mater. 24 (2020) 329–335.
[10] F. Wu, S.X. Wu, R.J. Chen, et al., Chin. Chem. Lett. 20 (2009) 1255–1258.
[11] H. Ye, D. Lei, L. Shen, et al., Chin. Chem. Lett. 31 (2020) 570–574.
[12] X. Shan, Y. Zhong, L. Zhang, et al., J. Phys. Chem. C 125 (2021) 19060–19080.
[13] B. Liu, Y. Zhang, Z. Wang, et al., Adv. Mater. 32 (2020) 2003657.
[14] Y.H. Lee, J.H. Kim, J.H. Kim, et al., Adv. Funct. Mater. 28 (2018) 1870293.
[15] K. Chen, R. Fang, Z. Lian, et al., Energy Stor. Mater. 37 (2021) 224–232.
[16] J. Wang, Y. Cui, D. Wang, Adv. Mater. 31 (2019) 1801993.
[17] R. Pongilat, K. Nallathamby, ACS Appl. Mater. Interfaces 10 (2018) 38853–38861.
[18] J.F. Zheng, M.B. Zheng, N.W. Li, et al., Chin. J. Inorg. Chem. 29 (2013) 1355–1360.
[19] D. Xiao, C. Lu, C. Chen, S. Yuan, Energy Stor. Mater. 10 (2018) 216–222.
[20] J. Guo, Y. Xu, C. Wang, Nano Lett. 11 (2011) 4288–4294.
[21] Y. Yang, C. Chen, J. Hu, et al., Chin. Chem. Lett. 29 (2018) 1777–1780.
[22] B. Liu, R. Fang, D. Xie, et al., Energy Environ. Mater. 1 (2018) 196–208.
[23] S. Jiang, S. Huang, M. Yao, et al., Chin. Chem. Lett. 31 (2020) 2347–2352.
[24] S. Han, D. Wu, S. Li, et al., Adv. Mater. 26 (2014) 849–864.
[25] Y. Qu, Z. Zhang, X. Zhang, et al., Carbon 84 (2015) 399–408.
[26] T. Wang, J. Zhu, Z. Wei, et al., Nano Lett. 19 (2019) 4384–4390.
[27] H. Wu, J. Lin, J. Mou, et al., RSC Adv. 7 (2017) 47407–47415.
[28] S. Shen, R. Zhou, Y. Li, et al., Small Methods 3 (2019) 1900596.
[29] Y. Zhong, X. Xia, S. Deng, et al., Adv. Mater. 30 (2018) 1805165.
[30] S. Shen, X. Xia, Y. Zhong, et al., Adv. Mater. 31 (2019) 1900009.
[31] M. Xu, M. Jia, C. Mao, et al., Sci. Rep. 6 (2016) 18739.
[32] S. Krishnan, E.K. Manavathu, P.H. Chandrasekar, Mycoses 52 (2009) 206–222.
[33] R.M. Apetrei, G. Carac, G. Bahrim, et al., Bioelectrochemistry 121 (2018) 46–55.
[34] J. Wang, F. Xiong, H. Liu, et al., Bioelectrochemistry 129 (2019) 10–17.
[35] E. Binkauskienė, V. Jasulaitienė, A. Lugauskas, Synth. Met. 159 (2009) 1365–1368.
[36] P. Yi, K. Xiao, C. Dong, et al., Bioelectrochemistry 119 (2018) 203–210.
[37] Y.P. Xie, H.W. Cheng, W. Chai, et al., Chin. Chem. Lett. 28 (2017) 738–742.
[38] H. Huang, J. Liu, Y. Xia, et al., J. Alloys Compd. 706 (2017) 227–233.
[39] J. Zhao, Z. Yan, J. Alloys Compd. (2020) 156609.
[40] H.J. Peng, G. Zhang, X. Chen, et al., Angew. Chem. Int. Ed. 55 (2016) 12990–12995.
[41] Y. Zhang, P. Zhang, S. Zhang, et al., InfoMat 3 (2021) 790–803.
[42] W. Chen, H. Jin, S. Xie, et al., J. Energy Chem. 54 (2021) 16–22.
[43] B. Guan, X. Sun, Y. Zhang, et al., Chin. Chem. Lett. 32 (2021) 2249–2253.
[44] J. Cheng, D. Zhao, L. Fan, et al., J. Mater. Chem. A 5 (2017) 14519–14524.
[45] Z. Guang, Y. Huang, X. Chen, et al., Electrochim. Acta 307 (2019) 260–268.
[46] H. Yuan, X. Chen, G. Zhou, et al., ACS Energy Lett. 2 (2017) 1711–1719.
[47] W. Cai, G. Li, K. Zhang, et al., Adv. Funct. Mater. 28 (2018) 1704865.
[48] Y. Shen, Y. Li, S. Deng, et al., Chin. Chem. Lett. 31 (2020) 846–850.
[49] H.J. Liu, J. Wang, C.X. Wang, Y.Y. Xia, Adv. Energy Mater. 1 (2011) 1101–1108.
[50] Y. Wang, M. Batmunkh, H. Mao, et al., Chin. Chem. Lett. 33 (2022) 394–398.
[51] Z.H. Sheng, L. Shao, J.J. Chen, et al., ACS Nano 5 (2011) 4350–4358.
[52] Z. Liu, L. Wang, W. Yang, Chin. Chem. Lett. 32 (2021) 2919–2922.
[53] Y. Zhong, X. Xia, S. Deng, et al., Adv. Energy Mater. 8 (2018) 1701110.
[54] B. Liu, Y. Zhang, Z. Wang, et al., Adv. Mater. 32 (2020) 2003657.
[55] X. Zhang, K. Huo, H. Wang, et al., ACS Appl. Mater. Interfaces 4 (2012) 1037–1042.
[56] H. Hou, X. Qiu, W. Wei, et al., Adv. Energy Mater. 7 (2017) 1602898.
[57] Y. Song, X. Li, C. He, Chin. Chem. Lett. 32 (2021) 1106–1110.
[58] J. Xu, N. Yang, S. Heuser, et al., Adv. Energy Mater. 9 (2019) 1803623.
[59] Z. Cui, J. Yao, T. Mei, et al., Electrochim. Acta 298 (2019) 43–51.
[60] X. Yuan, L. Cheng, L. Kong, et al., J. Alloys Compd. 596 (2014) 132–139.
[61] W. Bao, L. Liu, C. Wang, et al., Adv. Energy Mater. 8 (2018) 1702485.
[62] F. Xiao, X. Yang, H. Wang, et al., Adv. Energy Mater. 10 (2020) 2000931.
[63] Q. Pang, J. Tang, H. Huang, et al., Adv. Mater. 27 (2015) 6021–6028.
[64] J. Xu, W. Zhang, H. Fan, et al., Nano Energy 51 (2018) 73–82.
[65] X. Liang, C. Hart, Q. Pang, et al., Nat. Commun. 6 (2015) 5682.
[66] Y. Chen, S. Niu, W. Lv, et al., Chin. Chem. Lett. 30 (2019) 521–524.
[67] J. Liu, A. Wei, G. Pan, et al., Nano-Micro Lett. 11 (2019) 64.